Recognition of Histone H3 Lysine-4 Methylation by the Double Tudor Domain of JMJD2A

Ying Huang,[1*] Jia Fang,[2] Mark T. Bedford,[3] Yi Zhang,[2] Rui-Ming Xu[1*†]

Biological responses to histone methylation critically depend on the faithful readout and transduction of the methyl-lysine signal by "effector" proteins, yet our understanding of methyl-lysine recognition has so far been limited to the study of histone binding by chromodomain and WD40-repeat proteins. The double tudor domain of JMJD2A, a Jmjc domain–containing histone demethylase, binds methylated histone H3-K4 and H4-K20. We found that the double tudor domain has an interdigitated structure, and the unusual fold is required for its ability to bind methylated histone tails. The cocrystal structure of the JMJD2A double tudor domain with a trimethylated H3-K4 peptide reveals that the trimethyl-K4 is bound in a cage of three aromatic residues, two of which are from the tudor-2 motif, whereas the binding specificity is determined by side-chain interactions involving amino acids from the tudor-1 motif. Our study provides mechanistic insights into recognition of methylated histone tails by tudor domains and reveals the structural intricacy of methyl-lysine recognition by two closely spaced effector domains.

Posttranslational modifications of histones have a profound influence on fundamental biological processes such as transcriptional regulation and epigenetic inheritance (*1*, *2*). However, the mechanisms by which covalent histone modifications are recognized and deciphered remain poorly understood. Currently, both the recognition of acetylated histones by the bromo domain (*3*, *4*) and the binding of methylated histone tails by the chromo domain and a WD40-repeat protein, WDR5, are the only modified histone/protein interactions understood in any detail (*5*–*10*). The chromodomain is a member of the tudor domain "royal family," which includes the tudor, plant Agenet, chromo, PWWP, and MBT domains. Many of the proteins containing these domains are associated with chromatin (*11*). Using a protein-array approach, we recently showed that in addition to chromo domains, certain tudor and MBT domains specifically bind to methylated histone tails (*12*). Here we focus on the tudor domains of JMJD2A, which is a member of a conserved family of Jmjc domain–containing proteins (Fig. 1, A and B) belonging to the Jmjc domain histone demethylase superfamily (*13*). JMJD2A has been reported to interact with histone deacetylase complexes and Rb and to function as a transcription repressor (*14*, *15*).

Previous structural studies of the tudor domain of survival motor neuron (SMN) revealed that it contains a binding site for a symmetrically dimethylated arginine (*16*). The double tudor domain of 53BP1, a p53 binding protein, has been implicated in binding methylated Lys^{79} of histone H3 (*17*), methylated Lys^{20} of histone

[1]W. M. Keck Structural Biology Laboratory, Cold Spring Harbor Laboratory, Cold Spring Harbor, NY 11724, USA. [2]Howard Hughes Medical Institute and Department of Biochemistry and Biophysics, Lineberger Comprehensive Cancer Center, University of North Carolina at Chapel Hill, Chapel Hill, NC 27599–7295, USA. [3]The University of Texas M. D. Anderson Cancer Center, Science Park-Research Division, Post Office Box 389, Smithville, TX 78957, USA.

*Present address: Structural Biology Program, Skirball Institute of Biomolecular Medicine and Department of Pharmacology, New York University School of Medicine, New York, NY 10016, USA.

†To whom correspondence should be addressed. E-mail: rmxu@saturn.med.nyu.edu

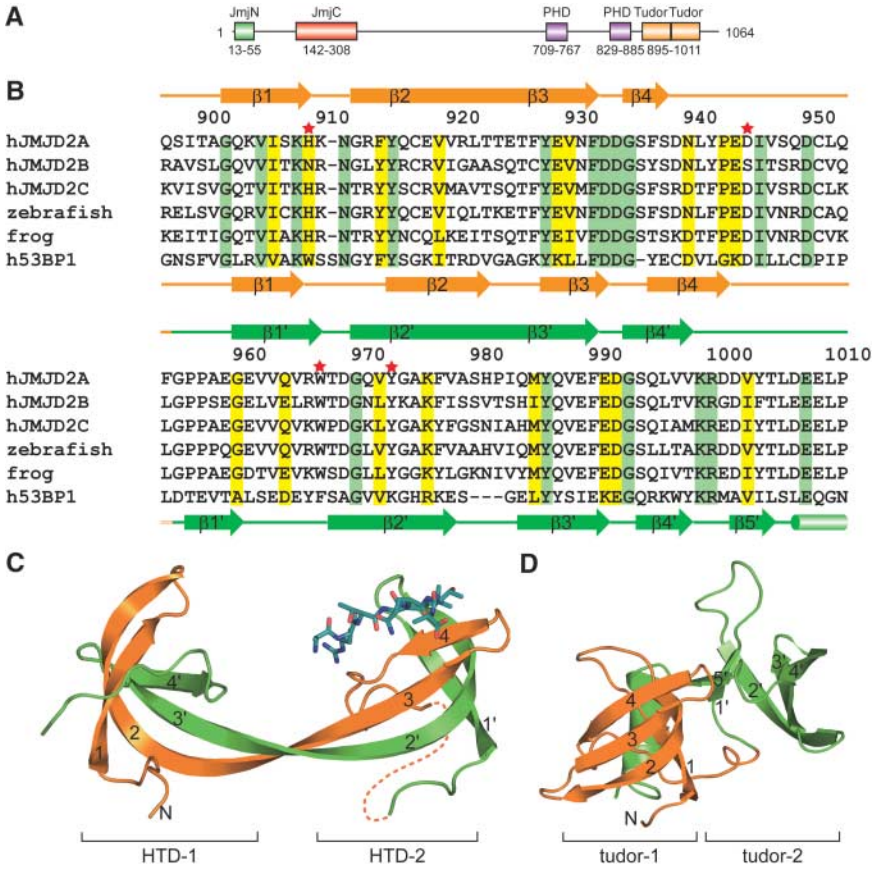

Fig. 1. JMJD2A structure. (**A**) A schematic drawing of the domain structure of JMJD2A. (**B**) Alignment of the double tudor domain sequences of three human JMJD2 homologs, one from zebrafish (Ensemble ID: DARP00000024692) and another from frog (Ensemble ID: XETP00000001152), and human 53BP1. Secondary-structure elements (orange and green for the first and second tudor motifs, respectively), their nomenclature, and the amino acid numbering of JMJD2A are shown above the sequences. The secondary-structure elements of the 53BP1 double tudor domain are delineated below the sequences. JMJD2A residues subjected to mutational studies are indicated by stars. (**C**) The structure of the JMJD2A double tudor domain (ribbon representation) in complex with a trimethylated H3K4 peptide (ball-and-stick model). Regions spanning the first and second tudor motifs are colored orange and green, respectively. The dotted line indicates a segment of seven disordered residues. (**D**) The structure of the double tudor domain of 53BP1 shown in a ribbon representation. Secondary-structure elements in (C) and (D) are colored as in (B).

H4 (*12*), as well as DNA and arginine-glycine–rich sequences (*18*). However, the structural basis for ligand binding by tudor domains is not understood. JMJD2A contains two tandem tudor domains, and the double tudor domain is known to bind methylated histone H3-K4 or H4-K20 (*12*). To gain insights into the structural basis for binding methylated histone tails, we have solved the crystal structure of the double tudor domain of JMJD2A both in the presence and absence of a trimethylated H3-K4 peptide (H3K4Me3). A detailed description of structure determination and data statistics can be found in the supporting online material.

Surprisingly, the 2.1 Å structure revealed that the two tudor domains interdigitate and form a bilobal, saddle-shaped structure with each lobe resembling the canonical tudor domain structure (Fig. 1C). We term these tudorlike lobes hybrid tudor domain 1 and 2 (HTD-1 and HTD-2). The methyl-H3-K4 peptide is bound in a cleft of HTD-2 (Fig. 1C). The interdigitated folding of the double tudor domain of JMJD2A differs appreciably from the structure of the homologous double tudor domain of 53BP1, which comprises two independently folded tudor domains (Fig. 1D) (*17*, *18*). The hybrid-tudor domains are formed by the exchange of the third and fourth β strands with respect to the canonical tudor domain. The swapped β3 forms a long, contiguous strand with the nonswapped β2, which we call β2β3, and the two long strands, β2β3 and β2'β3' (an apostrophe indicates secondary-structure elements of the second tudor motif, as denoted in Fig. 1B), bridge the two compact HTDs (Fig. 1, B and C).

Compared to the corresponding surface area of HTD-1, the surface of HTD-2 surrounding a cluster of aromatic residues has a more negatively charged electrostatic potential, consistent with its role in binding the positively charged H3K4Me3 peptide (Fig. 2A). Three aromatic residues, Trp^{967} and Tyr^{973} of the tudor-2 motif and Phe^{932} of the tudor-1 motif, form an open cage that accommodates the binding of trimethylated Lys^4 (Fig. 2B). The binding buries a total accessible surface area of 1039 $Å^2$. In addition, a negatively charged residue, Asp^{934}, lines up at the edge of the aromatic cage (Fig. 2C). This arrangement of aromatic residues and the negatively charged amino acid is reminiscent of the H3K9Me3 binding site of the HP1 chromo domain (Fig. 2B) (*5*, *6*). The aromatic cage is required for binding methylated lysines: Changing Tyr^{973} to an alanine (Y973A) or Trp^{967} to a histidine (W967H) abolishes the binding of H3K4Me3, whereas the wild-type double tudor domain binds the peptide with an apparent equilibrium dissociation constant (K_d) of 10.4 μM. The binding constants were determined using surface plasmon resonance (SPR) (Fig. 3, A and B).

A number of side chain-side chain interactions between HTD-2 and the H3K4Me3 peptide contribute to their binding specificity. In contrast to the binding of methylated histone peptides by chromo domains (*5*–*9*), there are only two β sheet–like main-chain hydrogen bonds between the H3K4Me3 peptide and HTD-2, which involve the main-chain atoms of Gln^5 of the histone peptide and Phe^{937} of HTD-2. In the present structure, Arg^2 of the histone H3 peptide interacts with Asp^{945} of HTD-2 through ionic and hydrogen bonds (Fig. 2C). Thr^3 of the peptide forms a hydrogen bond with Asn^{940}, and the peptide Gln^5 interacts with Phe^{937} through van der Waals contacts. In addition, the terminal amino group of the peptide interacts with HTD-2 through two weak hydrogen bonds (both ~3.4 Å), one with the hydroxyl group of Tyr^{942} and another with the carbonyl group of Ala^{941}. It should be noted that all of the HTD-2 residues involved, except the ones in the methyl-lysine binding aromatic cage, belong to the tudor-1 motif (Fig. 2C), which explains the observation that tudor-2 alone cannot bind H3K4Me3 (Fig. 3B).

Because Arg^2 of the H3K4Me3 peptide plays a prominent role in the interaction with the double tudor domain of JMJD2A, we tested the binding effect of mutations of Arg^2 and its interaction partner, Asp^{945} of HTD-2, by changing Arg^2 to an alanine (R2A) and changing Asp^{945} to an alanine (D945A) or an arginine (D945R). The wild-type double tudor domain binds the R2A H3K4Me3 peptide with a K_d of 127.9 μM, which is ~$^1/_{12}$th the level of binding to the wild-type H3K4Me3 peptide (Fig. 3). The D945A mutant binds to the wild-type H3K4Me3 peptide with a K_d of 118.4 μM, a level comparable to that between the wild-type double tudor domain and the R2A H3K4Me3 peptide, and the D945R mutant no longer binds the peptide. In the vicinity of Lys^9, Lys^{27}, and Lys^{36} of histone H3, either an alanine or a glycine occupies the position corresponding to that of Arg^2 (Fig. 3D). These small residues cannot efficiently interact with Asp^{945} of JMJD2A, which is likely to account for the preferential binding of the JMJD2A double tudor domain to H3K4Me3 over other histone H3 methyl-lysine marks.

As pointed out earlier, the double tudor domain can also bind methylated H4-K20 (*12*). A trimethylated H4-K20 peptide binds the double tudor domain of JMJD2A with a K_d of ~25 μM, and our study shows that the same binding pocket is involved in binding H3K4Me3 and methylated H4-K20, because the W967H and Y973A HTD-2

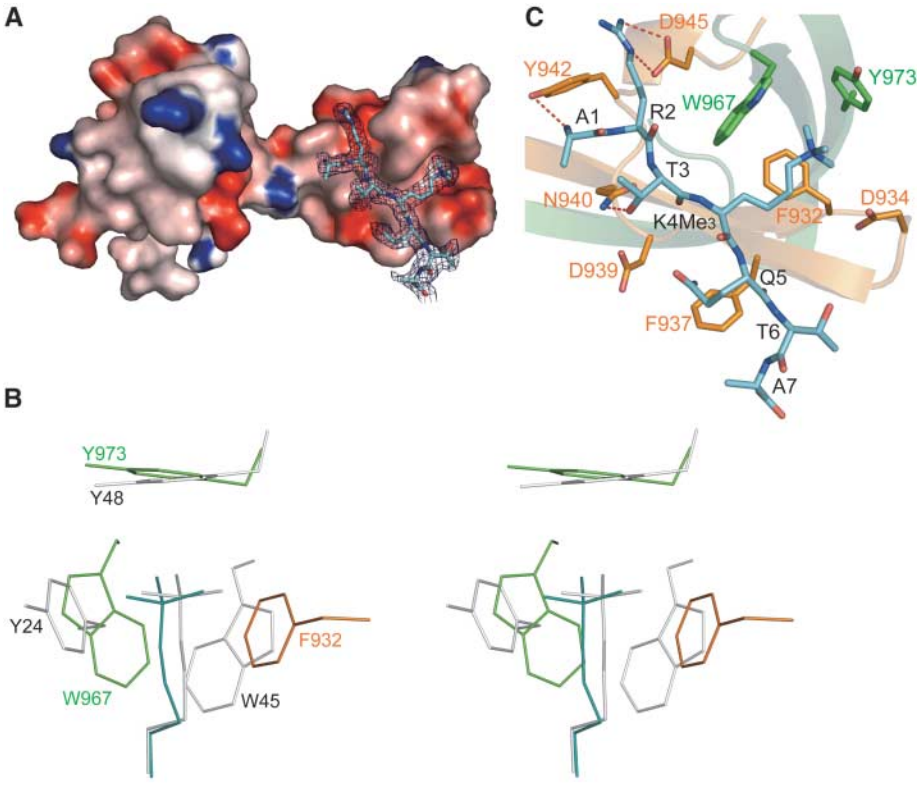

Fig. 2. JMJD2A double tudor domain–H3K4Me3 peptide interactions. (**A**) The double tudor domain as seen in a surface representation with electrostatic potential distribution colored red for negatively charged, white for neutral, and blue for positively charged areas. The peptide is shown as a stick model superimposed with the surrounding $2F_o - F_c$ electron density map (displayed at 1.2σ contour level). (**B**) A stereo view of the methyl-H3K4 (colored cyan) binding aromatic cage superimposed with the methyl-lysine binding aromatic cage of the chromo domain of HP1 (gray). Tudor-1 and Tudor-2 residues are colored orange and green, respectively. (**C**) A detailed view of JMJD2A-H3K4Me3 interactions. The peptide and the HTD-2 residues involved are shown in a stick model. Dashed lines indicate hydrogen bonds. The same coloring scheme as in Fig. 1 is used.

aromatic cage mutants also lost the ability to bind methylated H4-K20. In a H4-K20 peptide, the residue corresponding to Arg^2 is a histidine (Fig. 3D), which cannot interact with Asp^{945} as does Arg^2 of histone H3 but should still be able to bind favorably in the area formed by Leu^{941}, Tyr^{942}, and Asp^{945} (Fig. 2C). Furthermore, the HTD-2 region surrounding the methyl-lysine binding site is quite negatively charged (Fig. 2A), which provides a favorable environment for the binding of three positively charged arginine residues near H4-K20 (Fig. 3D).

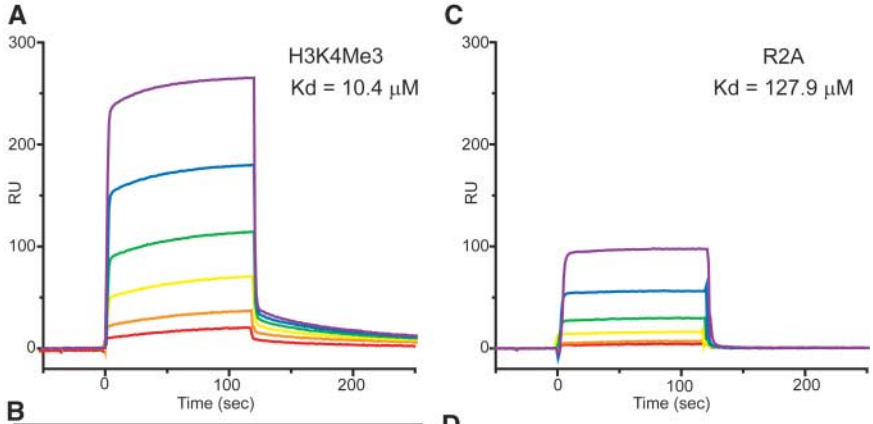

B

Protein	Immob. Peptide	Kd (μM)
wt	Btn-H3K4Me3	10.4
wt	Btn-H3K4	n/d
Y973A	Btn-H3K4Me3	n/d
W967H	Btn-H3K4Me3	n/d
W967H/H909W	Btn-H3K4Me3	n/d
Tudor2	Btn-H3K4Me3	n/d
D945A	Btn-H3K4Me3	118.4
D945R	Btn-H3K4Me3	n/d
wt	Btn-R2A	127.9

D

	-2	0
H3K4	A	RTKQTA
H3K9	T	ARKSTG
H3K27	A	ARKSAP
H3K36	G	GVKKPH
H4K20	R	HRKVLR

Fig. 3. Binding of the JMJD2A double tudor domain to histone H3 peptides. (**A**) Representative binding curves for the wild-type double tudor domain and a biotinylated H3K4Me3 peptide (Btn-H3K4Me3) as measured using SPR. Curves represent measurements with an increasing concentration of the protein used. From bottom to top: 1 μM (red), 2 μM (orange), 5 μM (yellow), 10 μM (green), 20 μM (blue), and 40 μM (magenta). The vertical and horizontal axes show the Biacore response unit (RU) and the time scale (seconds). (**B**) Tabulation of pairwise protein-peptide interactions measured. The wild-type or mutant JMJD2A double tudor domains used are shown in the first column, and the peptide used is indicated in the second column. Btn-H3K4: an H3K4 peptide with an unmethylated Lys^4; Btn-R2A: an H3K4Me3 peptide with an alanine in place of Arg^2. The derived equilibrium dissociation constants are shown in the third column, where n/d denotes bindings too weak to be reliably quantitated. (**C**) Representative binding curves of the wild-type double tudor domain with the Btn-R2A peptide. (**D**) Alignment of amino acid sequences encompassing known methylated lysine residues of histone H3 and H4. The position of methyl-lysines is designated position 0. Both the 0 and −2 positions are highlighted in red.

The two HTDs share ~23 and ~44% sequence identity and similarity, respectively, and the main chains of the two domains can be superimposed with a root mean square (RMS) deviation of 1.05 Å. In particular, a HTD-1 aromatic cage differs from that of HTD-2 only by one residue, a histidine (His^{909}) instead of a tryptophan (Trp^{967}). Superimposition of the two HTD domains reveals that His^{909} occupies a position that occludes the binding of a methyl-lysine (Fig. 4A). To determine whether His^{909} is solely responsible for the inability of HTD-1 to bind H3K4Me3, we changed the histidine to a tryptophan while at the same time changing Trp^{967} of HTD-2 to a histidine. As described earlier, the latter mutation alone precludes HTD-2 from binding H3K4Me3. The W967H/H909W double mutant does not bind H3K4Me3 (Fig. 3B). Thus, residues outside the aromatic cage are also important for the functional differences between HTD-1 and HTD-2. It is possible that HTD-1 could be involved in binding yet unidentified ligands.

There is little conformational change between the H3K4Me3 bound and free double tudor domain structures of JMJD2A, showing that the interdigitated structure is not due to H3K4Me3 binding and that conformational dynamics do not play a major role in regulating histone binding (fig. S1). HTDs and canonical tudor domains have similar secondary structural arrangements: HTD-1 and HTD-2 can be superimposed with the tudor domain of SMN (*16*) with RMS deviations of 1.26 and 0.87 Å, respectively. The locations of the aromatic cages in both HTDs also generally coincide with the sites in SMN and 53BP1 implicated in binding dimethylated arginine and methylated histone H3-K79, respectively (*16*, *17*). A comparison of the tudor domain structures reveals that the loop connecting β1 and β2, in which two of the three aromatic residues reside, has the most notable conformational variation among

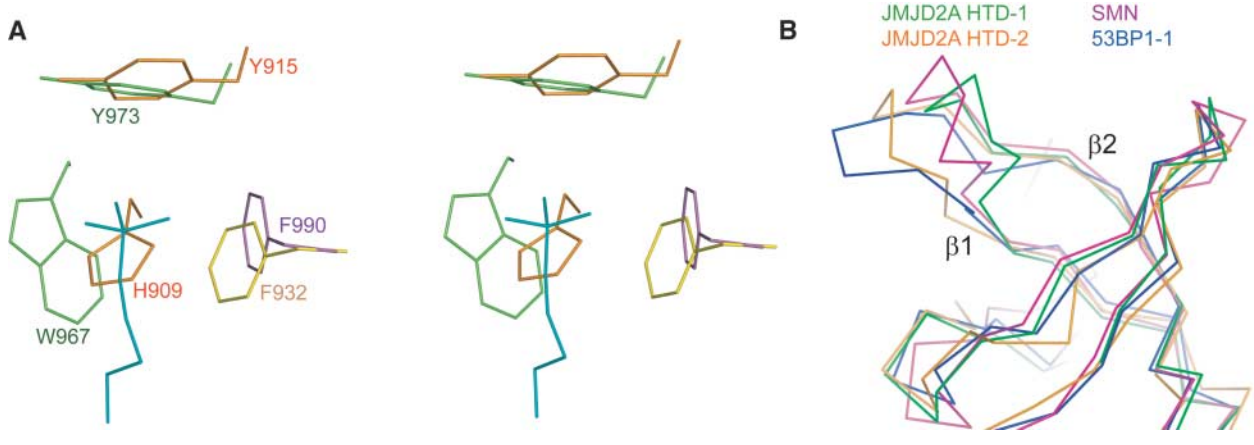

Fig. 4. Tudor domain ligand binding sites. (**A**) A stereo view of superimposed HTD-2 and HTD-1 aromatic clusters. The latter is formed by His^{909} and Tyr^{915} of the tudor-1 motif (orange) and Phe^{990} of tudor-2 (magenta). His^{909} clashes with the superimposed methyl-H3K4. (**B**) Conformational differences of the β1-β2 loop among HTD-1 (green) and HTD-2 (orange) of JMJD2A, SMN tudor (magenta), and the first tudor domain of 53BP1 (blue). Two of the aromatic residues implicated in binding methylated lysine, or arginine for SMN tudor, reside in this loop.

different tudor domains (Fig. 4B), perhaps reflecting the structural flexibility needed for accommodating different binding partners.

Because of the involvement in transcription regulation, it is tempting to speculate that the double tudor domain is responsible for directing JMJD2A to chromatin regions enriched with H3-K4 or H4-K20 methylation. However, alternative scenarios are also possible, and the functional relation between methyl-histone binding by the double tudor domain and histone demethylation by JMJD2A in a physiological context remains to be established. Nevertheless, our results demonstrate that the hybrid-tudor domain structure of JMJD2A is required for the formation of a functional methyl-histone H3 binding module. The unusual fold requires two tudor domain motifs in tandem, which is only present in a subset of tudor domain–containing proteins including JMJD2 family members and 53BP1. It will be extremely interesting to understand the principle underlying the distinct folding of the double tudor domains of JMJD2A and 53BP1 despite their sequence similarity. Many chromatin-associated proteins have closely spaced tandem repeats of effector domains implicated in histone binding, including the bromo, chromo, MBT, Agenet, and tudor domains. Our discovery reveals the potential for forming novel histone binding modules from the familiar effector domains.

References and Notes

1. T. Jenuwein, C. D. Allis, *Science* **293**, 1074 (2001).
2. C. Martin, Y. Zhang, *Nat. Rev. Mol. Cell Biol.* **6**, 838 (2005).
3. C. Dhalluin *et al.*, *Nature* **399**, 491 (1999).
4. R. H. Jacobson, A. G. Ladurner, D. S. King, R. Tjian, *Science* **288**, 1422 (2000).
5. S. A. Jacobs, S. Khorasanizadeh, *Science* **295**, 2080 (2002).
6. P. R. Nielsen *et al.*, *Nature* **416**, 103 (2002).
7. J. Min, Y. Zhang, R. M. Xu, *Genes Dev.* **17**, 1823 (2003).
8. W. Fischle *et al.*, *Genes Dev.* **17**, 1870 (2003).
9. J. F. Flanagan *et al.*, *Nature* **438**, 1181 (2005).
10. J. Wysocka *et al.*, *Cell* **121**, 859 (2005).
11. S. Maurer-Stroh *et al.*, *Trends Biochem. Sci.* **28**, 69 (2003).
12. J. Kim *et al.*, *EMBO Rep.* **7**, 397 (2006).
13. Y.-i. Tsukada *et al.*, *Nature* **439**, 811 (2006).
14. D. Zhang, H. G. Yoon, J. Wong, *Mol. Cell. Biol.* **25**, 6404 (2005).
15. S. G. Gray *et al.*, *J. Biol. Chem.* **280**, 28507 (2005).
16. R. Sprangers, M. R. Groves, I. Sinning, M. Sattler, *J. Mol. Biol.* **327**, 507 (2003).
17. Y. Huyen *et al.*, *Nature* **432**, 406 (2004).
18. G. Charier *et al.*, *Structure* **12**, 1551 (2004).

19. We thank D. Schneider and A. Heroux for help at the X26C beamline of the National Synchrotron Light Source (Brookhaven National Laboratory), and L. Henry and S. Shaw for comments on the manuscript. The coordinates and the structure factors have been deposited with the RCSB (Research Collaboratory for Structural Bioinformatics) Protein Data Bank with accession codes 2GFA (H3K4Me3 bound) and 2GF7 (free). The work was supported in part by the W. M. Keck foundation (R.-M.X.), the Howard Hughes Medical Institute (Y.Z.), and NIH grants GM 63718 (R.M.X.), GM68804 (Y.Z.), and DK62248 (M.T.B.). Y.Z. is an Investigator of the Howard Hughes Medical Institute.

Supporting Online Material

www.sciencemag.org/cgi/content/full/1125162/DC1
Materials and Methods
Fig. S1
Table S1
References

19 January 2006; accepted 27 March 2006
Published online 6 April 2006;
10.1126/science.1125162
Include this information when citing this paper.

The Embryonic Vertebrate Heart Tube Is a Dynamic Suction Pump

Arian S. Forouhar,[1] Michael Liebling,[2] Anna Hickerson,[1] Abbas Nasiraei-Moghaddam,[1] Huai-Jen Tsai,[4] Jay R. Hove,[5] Scott E. Fraser,[1,2] Mary E. Dickinson,[2,6] Morteza Gharib[1,3]*

The embryonic vertebrate heart begins pumping blood long before the development of discernable chambers and valves. At these early stages, the heart tube has been described as a peristaltic pump. Recent advances in confocal laser scanning microscopy and four-dimensional visualization have warranted another look at early cardiac structure and function. We examined the movement of cells in the embryonic zebrafish heart tube and the flow of blood through the heart and obtained results that contradict peristalsis as a pumping mechanism in the embryonic heart. We propose a more likely explanation of early cardiac dynamics in which the pumping action results from suction due to elastic wave propagation in the heart tube.

The cardiovascular system is the first functional organ system to develop in vertebrate embryos. In its earliest stages, it consists of a primitive heart tube that drives blood through a simple vascular network. Cardiac physiologists have long conjectured that the valveless embryonic heart tube drives circulation by means of peristaltic contractions (*1*, *2*), a pumping mechanism that pushes blood through the heart tube by progressively reducing the tube volume (*3*). Confirmation of this pumping mechanism requires in vivo visualization and quantification of both heart wall motion and blood cell motion, which are difficult with traditional imaging modalities. The zebrafish offers a powerful vertebrate model for cardiogenetic studies (*4*–*7*) with multiple advantages for in vivo imaging: Eggs are externally fertilized; embryos are nearly transparent, providing optical access to the earliest stages of cardiogenesis; and many GFP (green fluorescent protein)-labeled transgenic strains have been derived.

Recent improvements in confocal microscopy and four-dimensional (three spatial dimensions plus time) reconstruction protocols (*8*) permit us to take full advantage of these qualities and revisit the pumping mechanism of the early embryonic heart tube. We tested three implications of peristaltic pumping in the heart, namely that (i) there should be a unidirectional wave traveling along the endocardial layer, (ii) blood cell velocities should be bounded in magnitude by the instantaneous traveling wave speed through the heart tube wall, and (iii) cardiac output should increase linearly with heart rate.

To test the nature of cardiac pumping, we used in vivo high-speed confocal imaging of zebrafish hearts before valve formation. Optical sections through 26–hours postfertilization (hpf) *Tg(gata1:GFP)* zebrafish hearts expressing GFP in blood cells, endocardium, and myocardium were reconstructed into four-dimensional data sets (*8*) (Fig. 1A and movie S1), which provided direct three-dimensional data on the position of myocardial and endocardial cells throughout the cardiac cycle (Figs. 1B and 2 and movies S1 to S3). By tracking the position of the trailing edge of the endocardial wave crest during the cardiac cycle, we identified the speed and the direction of the traveling wave through the heart wall. The wave originates in myocardial cells positioned near the inflow tract of the heart tube (Fig. 2), and upon contraction a bidirectional wave propagates axially along the heart tube wall (Fig. 1 and movies S1 and S2). The proximity of the pacemaker cells to the venous boundary of the heart tube, along with the speed of the traveling wave, combine to make this bidirectional wave undetectable through traditional imaging modalities.

In a peristaltic heart tube model, the net flow is exactly equal to the volume displaced during contractions. This dynamic imposes a direct relationship between the upstream blood velocity and the local traveling wave velocity. Specifically, because peristalsis is governed by static pressure rather than dynamic pressure (*3*),

[1]Option in Bioengineering, [2]Biological Imaging Center, Beckman Institute, [3]Graduate Aeronautical Laboratories, California Institute of Technology (Caltech), Pasadena, CA 91125, USA. [4]Institute of Molecular and Cellular Biology, National Taiwan University, Taiwan. [5]Genome Research Institute, University of Cincinnati, Cincinnati, OH 45221, USA. [6]Department of Molecular Physiology and Biophysics, Baylor College of Medicine, Houston, TX 77030, USA.

*To whom correspondence should be addressed. E-mail: mgharib@caltech.edu